Broadband Sequential Load Modulated Balanced Amplifier With Extended Design Space Using Second Harmonic Manipulation

Chenhao Chu, *Member, IEEE*, Jingzhou Pang, *Senior Member, IEEE*, Ramzi Darraji, *Member, IEEE*, Sagar K. Dhar, *Member, IEEE*, Tushar Sharma, *Member, IEEE*, and Anding Zhu, *Fellow, IEEE*

***Abstract*— This article presents the design methodology of a broadband radio frequency (RF)-input sequential load modulated balanced amplifier (SLMBA) with extended high-efficiency design space, by introducing the second-harmonic load manipulation over an enlarged range for the control amplifier (CA). The extension of CA load design space not only can provide the time-domain-varying drain current waveform inside the entire design continuum but also allows maintaining high efficiency at output power back-off (OBO) over an extended operation bandwidth. To validate the theory, a broadband SLMBA operating at 2.05–3.65 GHz was designed and fabricated using packaged gallium nitride (GaN) transistors. The implemented power amplifier (PA) attains a measured 45.2–46.8-dBm peak output power. Drain efficiency (DE) of 61.2%–79.7% at saturation and 50.5%–66.2% at 8-dB OBO is achieved throughout the designed bandwidth. When tested with a 100-MHz long-term evolution (LTE) signal with a peak-to-average-power ratio (PAPR) of 8 dB, the proposed SLMBA achieves 50.7%–63.5% average DE over 2.05–3.55 GHz and better than −45.1 dBc adjacent channel power ratio (ACPR) after digital predistortion (DPD).**

***Index Terms*— Broadband, continuous-mode (CM), fifth generation (5G), harmonic manipulation, high efficiency, load modulated balanced amplifier (LMBA).**

I. Introduction

TO MEET demands for higher data rates and larger capacity, the fifth-generation (5G) communication system [1] will use new air interfaces with more frequency bands. In the meantime, the fourth-generation (4G) long-term evolution (LTE) bands will continue to be used in the 5G system [2], [3]. As such, there are tremendous demands for radio frequency (RF) power amplifiers (PAs) to operate with high efficiency over a wide dynamic power range in a wide range of frequency bands.

Doherty PA (DPA) has been widely used because of its enhanced efficiency at output power back-off (OBO) level. To increase the bandwidth, many techniques have been proposed, e.g., using modified load modulation networks [4], [5], [6], [7], [8], [9]. As the continuous-mode (CM) theory can expand the design space for RF PAs [10], [11], [12], [13], [14], [15], [16], [17], [18], [19], CM DPAs have also been proposed [20], [21], [22], [23], [24], [25], aiming to achieve high efficiency at OBO over wideband operation. However, with further increased bandwidth, the Doherty design becomes difficult.

The load modulated balanced amplifier (LMBA), a new PA architecture proposed recently, has the potential to overcome the bandwidth and OBO range limitations of DPAs [26], [27], [28], [29], [30], [31]. The CM-LMBA has shown load modulation trajectories in continuous characters using Class-B/J balanced amplifier (BA) as the carrier branch [32]. An RF-input sequential load modulated balanced amplifier (SLMBA) was also proposed [33], [34], where the control amplifier (CA) operates as the carrier branch while the BA becomes the peaking branch. Because there is no load modulation in the carrier branch, the CM CA can be designed to provide high efficiency at OBO over a wide bandwidth. Using the continuous Class-F^{-1} CA, the design space of the fundamental impedance of the BA can be extended by varying the second-harmonic load impedance of the CA [35], [36]. The recently reported hybrid asymmetrical load modulated balanced amplifier (H-ALMBA) also used harmonic-controlled output matching networks (OMNs) for the realization of hybrid continuous Class-F/F^{-1} CA operation in carrier branch [37].

In theory, the bandwidth of both the LMBA and SLMBA configurations is only constrained by the bandwidth of the input and output quadrature couplers [26], [33], [34], [38], [39]. However, in practice, the active devices of CA and BA cells require proper source/load fundamental or harmonic impedance tuning to achieve high efficiency with broadband operation [32], [35], [36], [37], [40], [41], [42], [43], [44], [45], [46]. Although the CM theory provides PA design with high-efficiency broadband load design continuum, a fundamental limitation exists that most of the practical

Manuscript received 5 June 2022; revised 10 October 2022; accepted 12 November 2022. Date of publication 12 December 2022; date of current version 5 May 2023. This work was supported in part by the Science Foundation Ireland under Grant 16/IA/4449 and Grant 17/NSFC/4850. *(Corresponding author: Chenhao Chu.)*

Chenhao Chu and Anding Zhu are with the School of Electrical and Electronic Engineering, University College Dublin, Dublin 4, D04 V1W8 Ireland (e-mail: chenhao.chu@ucdconnect.ie; anding.zhu@ucd.ie).

Jingzhou Pang is with the School of Microelectronics and Communication Engineering, Chongqing University, Chongqing 400044, China (e-mail: jingzhou.pang@cqu.edu.cn).

Ramzi Darraji is with Renesas Electronics Corporation, Ottawa, ON K2K 2M5, Canada (e-mail: rdarraji@ieee.org).

Sagar K. Dhar and Tushar Sharma are with Renesas Electronics Corporation, San Diego, CA 92014 USA (e-mail: sagar.dhar.vz@renesas.com; sharma.tushar17@ieee.org).

Color versions of one or more figures in this article are available at https://doi.org/10.1109/TMTT.2022.3226440.

Digital Object Identifier 10.1109/TMTT.2022.3226440

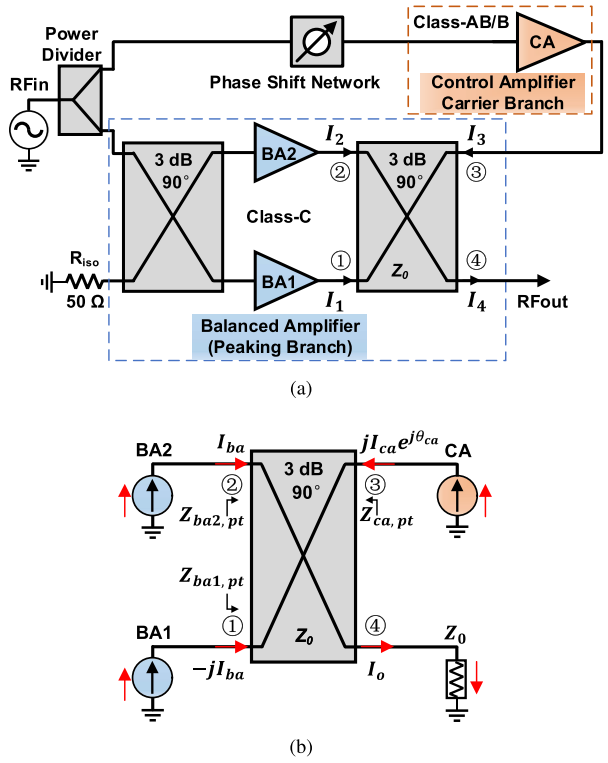

Fig. 1. Overview of RF-input SLMBA configuration. (a) General structure. (b) Theoretical block diagram for the analysis of output power combining.

transmission-line (TL)-based matching networks have some impedance mismatch when tracking the design space over a wide frequency band.

In this article, a broadband SLMBA is proposed with the CA operating in an extended high-efficiency CM design space via second-harmonic manipulation. Theoretical analysis shows that the extended CA fundamental load impedance design space not only can provide the time-domain-varying drain current waveform over the design continuum but also contributes to high output OBO efficiency in the proposed SLMBA. Case studies show that the combination of different OBO input driving levels and normalized CA second-harmonic voltage can provide the BA peaking branch with multiple sets of expanded fundamental design space (i.e., either along constant resistance contour or resistively extended contours). Different from the previous work on waveform engineered sequential load modulated balanced amplifier (W-SLMBA) [35], this work focuses on the further extension of broadband operation without deteriorating high efficiency at either OBO or saturation level.

The remaining part of the article is organized as follows. Section II presents the theory of the proposed SLMBA with extended high-efficiency CM design space. Section III shows the detailed design procedure. In Section IV, the experimental results and comparison to the existing LMBA/SLMBA configurations are represented. Finally, this article is concluded in Section V.

II. Theoretical Analysis

The SLMBA is an inverted architecture of the original LMBA. The general schematic of the RF-input SLMBA configuration is shown in Fig. 1(a), wherein a Class-AB/B biased CA is used as the carrier branch, and the BA composed of two Class-C biased PAs operates as the peaking branch. In the low power level, the BA is turned OFF, while the CA solely contributes to the output power for the entire SLMBA and is saturated at OBO. In the high power level, the CA remains saturated, while the BA starts to turn ON and will continue to provide the output power until it reaches saturation.

As shown in Fig. 1(b), the three amplifiers in SLMBA can be modeled by ideal current sources connected to the output quadrature coupler. According to the SLMBA theory introduced in [33] and [34], the port impedance for BA1 and BA2 can be represented as

$$Z_{\mathrm{ba1,pt}} = Z_{\mathrm{ba2,pt}} = Z_{\mathrm{ba,pt}} = Z_0\left(1+\sqrt{2}\frac{I_{\mathrm{ca}}}{I_{\mathrm{ba}}}e^{j\theta_{\mathrm{ca}}}\right) \quad (1)$$

wherein Z_0 is the characteristic impedance of the coupler, and $I_1 = -jI_{\mathrm{ba}}$ and $I_2 = I_{\mathrm{ba}}$ represent the currents of two cells (BA1 and BA2) in the BA branch with equal magnitude and quadrature phase difference. The control signal current is denoted as $I_3 = jI_{\mathrm{ca}}e^{j\theta_{\mathrm{ca}}}$. To ensure optimal power combining, the CA-BA phase shift is assumed to be $\theta_{\mathrm{ca}} = 0$.

The reported W-SLMBA [35] presented the expansion of BA fundamental port impedance design space by exploiting the varying CA fundamental current component $i_{\mathrm{ca}}[1]$ versus the second-harmonic load impedance $Z_{\mathrm{ca,2nd}}$ along the open-circuit region on the Smith chart. Such CA-BA harmonic fundamental control can only be realized using continuous Class-F^{-1} mode in the CA carrier branch, which might create difficulties when aiming for further extension of bandwidth in practical design. The continuous Class-F^{-1} theory generally provides only one single set of design space with constant fundamental conductance real($Y_{\mathrm{ca,1st}}$), while the TL-based OMN usually suffer from impedance mismatch when tracking the design space over the frequency domain [47], [48]. In consequence, more complex OMN structures might be required to track the fundamental and harmonic load design space precisely [35], which in return limits the maximum achievable bandwidth of the PA.

To mitigate the above-mentioned limitation, we revisited the intrinsic drain voltage and current waveforms. It is interesting to note that proper manipulation of second-harmonic load impedance $Z_{\mathrm{ca,2nd}}$ not only can generate different time-domain current waveform but also bring alteration to the time-domain drain voltage waveform. This provides a solution that can further extend the high-efficiency CA design space beyond the previously reported continuous Class-F^{-1} operation, via the manipulation of second harmonic. To obtain the performance of the proposed SLMBA configuration in detail, the effect from the proposed CA with second-harmonic manipulation and the behavior of the proposed SLMBA are analyzed below.

A. CA With Second-Harmonic Manipulation Overextended Range

It is known that manipulating the second-harmonic load impedance $Z_{\mathrm{ca,2nd}}$ can result in the amplitude change to the drain voltage of the transistor [10]. To better illustrate this manipulation and quantify the performance improvement,

in [10], the parameter k_2 is introduced and defined as the ratio of the second-harmonic component to the fundamental component of the CA drain voltage, namely, $k_2 = v_{\rm ca}[2]/v_{\rm ca}[1]$. Assuming the third harmonic is terminated to a short circuit, the generalized time-domain CA drain voltage waveform can be expressed as

$$v_{d,\rm ca}(\theta, k_2) = V_{\rm dc,ca} - v_{\rm ca}[1](\cos\theta + k_2 \cdot \cos 2\theta) \tag{2}$$

where $V_{\rm dc,ca}$ is the DC voltage, and $v_{\rm ca}[1]$ is the fundamental voltage. Meanwhile, as analyzed in [49] and [35], the shaped CA intrinsic drain current waveform varies as a function of second-harmonic load reactance imag $(Z_{\rm ca,2nd})$ and k_2.

Based on the analysis in [35], [47], and [49], the generalized time-domain drain current waveform of the CA, $i_{d,\rm ca}$, can be derived and expressed as

$$i_{d,\rm ca}(\theta) = \begin{cases} I_{\max,\rm ca}\cos\theta - \left(\dfrac{4I_{\max,\rm ca}}{3\pi}\cos 2\theta - \dfrac{2\delta(k_2)k_2 V_{\rm dck,ca}}{\text{imag}(Z\text{ca, 2nd})}\sin 2\theta\right), \\ \quad -\dfrac{\pi}{2} < \theta < \dfrac{\pi}{2} \\ 0, \quad -\pi < \theta < -\dfrac{\pi}{2}, \quad \dfrac{\pi}{2} < \theta < \pi \end{cases} \tag{3}$$

where $I_{\max,\rm ca}$ is the maximum current limit of the CA device and $V_{\rm dck,ca} = (V_{\rm dc,ca} - V_{\rm knee,ca})$. $V_{\rm dc,ca}$ and $V_{\rm knee,ca}$ are the drain supply voltage and device knee voltage, respectively. $\delta(k_2)$ is the voltage gain function and can be expressed according to the analysis in [10]

$$\delta(k_2) = \begin{cases} \dfrac{-1}{k_2 + \frac{1}{8\cdot k_2}}, & \text{if } k_2 \le -\dfrac{1}{4} \\ \dfrac{1}{1+k_2}, & \text{if } -\dfrac{1}{4} \le k_2 \le 0. \end{cases} \tag{4}$$

As the peak drain current $i_{d,\rm ca}$ excursion should not exceed $I_{\max,\rm ca}$, the second-harmonic load impedance $Z_{\rm ca,2nd}$ must be constrained by a boundary condition [18], [35], [49]. Such a condition with limit on $Z_{\rm ca,2nd}$ can be derived by referring equations (41)–(44) in [49]

$$i_{\rm ca}[2,q]^{\rm lim} \approx \pm 0.3 \cdot i_{\rm ca}[1,r] \tag{5}$$

wherein $i_{\rm ca}[n,r]$ and $i_{\rm ca}[n,q]$ $(n = 1, 2)$ represent the real and reactive current components, respectively, which can be calculated using the Fourier transformation of (3). Therefore, we can obtain the expression as

$$\frac{\delta(k_2)k_2 V_{\rm dck,ca}}{\text{imag}\,(Z\text{ca, 2nd})^{\rm lim}} \approx \pm 0.3 \cdot I_{\max,\rm ca} \cdot \left(\frac{1}{2} - \frac{8}{9\pi^2}\right). \tag{6}$$

Finally, the boundary condition of CA second-harmonic load impedance $Z_{\rm ca,2nd}$ can be obtained as

$$Z_{\rm ca,2nd}^{\rm lim} \approx \pm j \cdot \frac{8\delta(k_2)\cdot k_2 \cdot V_{\rm dck,ca}}{I_{\max,\rm ca}}. \tag{7}$$

Fig. 2(a) shows the CA drain voltage with high swing and the square-wave-shaped drain current waveform with $k_2 = -\sqrt{2}/4 \approx -0.35$, which is for the specific continuous Class-F^{-1}. In comparison, as shown in Fig. 2(b), when the value of k_2 changes, alternative drain voltage waveform swings can be provided with the same set of drain current waveforms. It is interesting to see that the drain voltage waveform is unchanged with alternative $Z_{\rm ca,2nd}$ and the drain current waveform keeps constant with different values of k_2. Therefore, the corresponding fundamental and second-harmonic load impedance continuum can be relaxed from the strict requirement from that of continuous Class-F^{-1}, resulting in an extended design space.

Since the proposed SLMBA can be described according to the normalized input driving level, β, where $0 \le \beta \le 1$, we define $\beta_{\rm bo}$ as the input driving level corresponding to OBO [32], [33], [35]. Herein, the CA design space is analyzed when it hits saturation, which is also at the OBO level with $\beta = \beta_{\rm bo}$ in the proposed SLMBA. According to (2)–(7), the intrinsic CA fundamental load impedance $Z_{\rm ca,1st}$ varies as a function of second-harmonic reactance imag $(Z_{\rm ca,2nd})$ and normalized drain voltage second-harmonic component k_2, and it can be expressed as

$$\begin{aligned} Z_{\rm ca,1st} &= -\frac{v_{\rm ca}[1]}{i_{\rm ca}[1]} \\ &= \frac{\delta(k_2)\cdot V_{\rm dck,ca}}{I_{\max,\rm ca}\left(\frac{1}{2} - \frac{8}{9\pi^2}\right) - j\cdot\frac{8}{3\pi}\frac{\delta(k_2)\cdot k_2\cdot V_{\rm dck,ca}}{\text{imag}\,(Z_{\rm ca,2nd})}}. \end{aligned} \tag{8}$$

Hence, the intrinsic CA fundamental admittance $Y_{\rm ca,1st}$ can be calculated as

$$Y_{\rm ca,1st} = \left(\frac{1}{2} - \frac{8}{9\pi^2}\right)\frac{I_{\max,\rm ca}}{V_{\rm dck,ca}}\frac{1}{\delta(k_2)} - j\cdot\frac{8}{3\pi}\frac{k_2}{\text{imag}\,(Z_{\rm ca,2nd})} \tag{9}$$

which shows that the intrinsic CA fundamental conductance can be varied along real axis on the Smith chart with proper control of k_2, corresponding to different values of CA second-harmonic impedance $Z_{\rm ca,2nd}$. When $k_2 = -0.35$, the operation described in (2)–(9) degenerates to that for the conventional continuous Class-F^{-1} PAs. Fig. 2(c) illustrates that the alternative value of k_2 can provide different sets of CA second-harmonic load impedance $Z_{\rm ca,2nd}$, which means the second-harmonic tuning range is extended, which, in return, provides more choices on the CA fundamental load impedance $Z_{\rm ca,1st}$ to extend high-efficiency CM operation.

Since only CA is turned ON when $\beta = \beta_{\rm bo}$, the OBO performance in terms of output power and efficiency can be expressed as [47]

$$\begin{aligned} P_{\rm obo} &= P_{\rm ca,sat} = \frac{\delta(k_2)\cdot V_{\rm dck,ca}}{\sqrt{2}}\cdot\frac{I_{\max,\rm ca}}{\sqrt{2}}\cdot\left(\frac{1}{2} - \frac{8}{9\pi^2}\right) \\ \eta_{\rm obo} &= \eta_{\rm ca,sat} = \frac{\pi}{2}\cdot\left(\frac{1}{2} - \frac{8}{9\pi^2}\right)\cdot\frac{\delta(k_2)\cdot V_{\rm dck,ca}}{V_{\rm dc,ca}}. \end{aligned} \tag{10}$$

To better illustrate the performance with the variation in normalized second-harmonic drain voltage k_2, the theoretical efficiency and output power are plotted in Fig. 3(a), using the configuration of $V_{\rm dck,ca} = V_{\rm dc,ca} = 20$ V and $I_{\max,\rm ca} = 1$ A as an example. With k_2 varying inside $[-0.5, -0.2]$, the extended high-efficiency CM design space for CA is established, where the efficiency varies from 80.0% to 91.0% while the output power varies from 37.1 to 37.6 dBm. It is worth to mention that not all the values of k_2 inside $[-0.5, -0.2]$ can be used for the

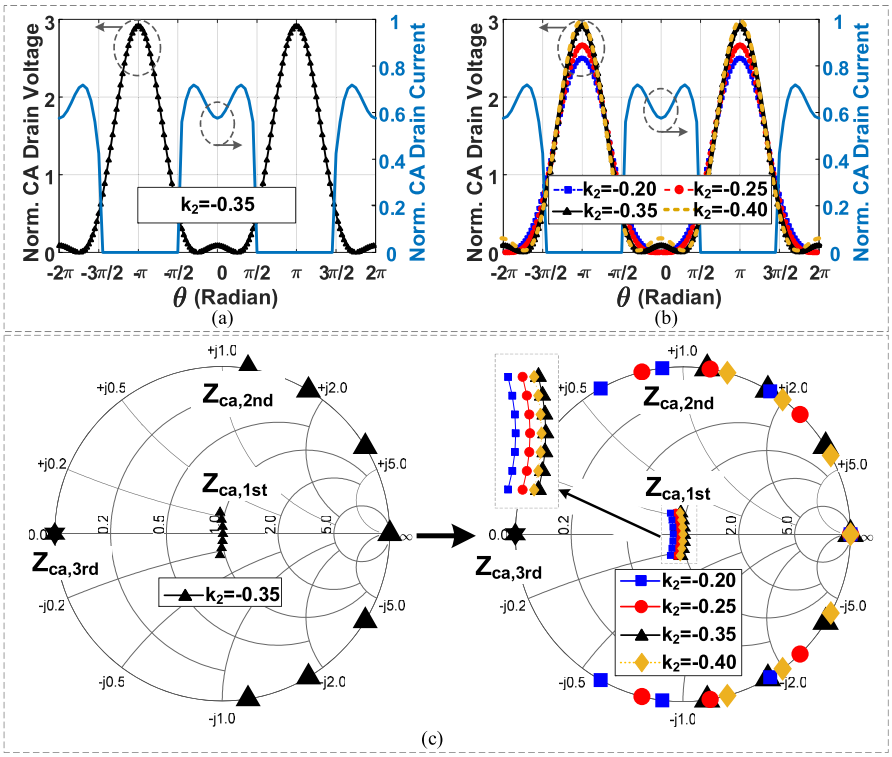

Fig. 2. (a) Normalized drain voltage (black curve) and current (blue curve) waveform with second-harmonic load impedance $Z_{\mathrm{ca,2nd}} = \infty$ when $k_2 = -0.35$. (b) Normalized drain voltage (colored curves) and current (blue curve) waveform versus different values of k_2, i.e., $k_2 = -0.20, -0.25, -0.35, and -0.40$. (c) Intrinsic design space for CA load impedance when $k_2 = -0.20, -0.25, -0.35, and -0.40$, respectively.

practical design. For example, for $-0.50 \le k_2 < -0.35$, the corresponding fundamental load design continuum overlaps with that for k_2 within the range of $[-0.35, -0.20]$, while the second-harmonic load impedance tuning rage is shrunk compared with that of $k_2 = -0.35$, as shown in Fig. 2(c). In this case, the normalized intrinsic drain voltage waveform exhibits an overshooting behavior at peaks along with high ripples at the minima, as shown in Fig. 3(b). This forces the device to operate near breakdown, which might impact its reliability. As a result, it is preferably to select the k_2 values within the range of $[-0.35, -0.20]$ to provide a good tradeoff in terms of voltage level at the peaks, ripples at the minima, and bandwidth extension in the high-efficiency design space.

B. BA Behavior Analysis

The BA starts to turn ON when the input power level β keeps increasing from β_{bo} at OBO level. To better analyze the performance of BA, we focus on the behavior at peak power level, where both CA and BA operate at the saturation with $\beta = 1$. Since two BA cells are biased in Class-C mode, the fundamental components of the BA current $i_{\mathrm{ba,peak}}[1]$ at peak power level can be calculated as [35]

$$\begin{aligned} i_{\mathrm{ba,peak}}[1] &= \left\{ \frac{1}{\pi} \int_{-\theta_b}^{\theta_b} I_{\mathrm{max,ba}} \frac{\beta \cdot \cos\theta - \beta_{\mathrm{bo}}}{1 - \beta_{\mathrm{bo}}} \cos\theta d\theta \right\} |_{\beta=1} \\ &= \frac{I_{\mathrm{max,ba}}}{1 - \beta_{\mathrm{bo}}} \cdot \frac{(2\theta_b + \sin 2\theta_b) - 4\beta_{\mathrm{bo}} \sin\theta_b}{2\pi} \end{aligned} \tag{11}$$

where $I_{\mathrm{max,ba}}$ is the maximum current limit of the BA device. $(-\theta_b, \theta_b)$ defines the turn-on phase range of the BA and θ_b can be obtained as

$$\theta_b = \arccos \frac{\beta_{\mathrm{bo}}}{\beta}. \tag{12}$$

The BA fundamental port impedance at saturation can be calculated as

$$\begin{aligned} Z_{\mathrm{ba,pt,1st}} &= Z_0 \left(1 + \sqrt{2} \frac{i_{\mathrm{ca}}[1]}{i_{\mathrm{ba}}[1]} \right) \\ &= Z_0 \left(1 + \sqrt{2} \left(\frac{1}{2} - \frac{8}{9\pi^2} \right) \cdot \frac{1}{\sigma} \cdot \frac{I_{\mathrm{max,ca}}}{I_{\mathrm{max,ba}}} \right. \\ &\quad \left. - j \cdot \frac{8\sqrt{2}}{3\pi} \cdot \frac{1}{\sigma} \cdot \frac{\delta(k_2) \cdot k_2 \cdot V_{\mathrm{dck,ca}}}{\mathrm{imag}\,(Z\mathrm{ca,\,2nd}) \cdot I_{\mathrm{max,ba}}} \right) \end{aligned} \tag{13}$$

where

$$\sigma = \frac{(2\theta_b + \sin 2\theta_b) - 4\beta_{\mathrm{bo}} \sin\theta_b}{2\pi(1 - \beta_{\mathrm{bo}})}. \tag{14}$$

Substituting (7) into (13), the reactive part of BA fundamental impedance varies in the range of

$$\left(-j \cdot \frac{\sqrt{2}}{3\pi} \cdot \frac{1}{\sigma} \cdot \frac{I_{\mathrm{max,ca}}}{I_{\mathrm{max,ba}}}, j \cdot \frac{\sqrt{2}}{3\pi} \cdot \frac{1}{\sigma} \cdot \frac{I_{\mathrm{max,ca}}}{I_{\mathrm{max,ba}}} \right). \tag{15}$$

From (13) to (15), it can be seen that the BA fundamental port impedance can be expanded due to the injection of the varying CA fundamental current which is shaped by the intrinsic CA second-harmonic reactance over the extended range. What is more, for the fixed CA and BA devices and

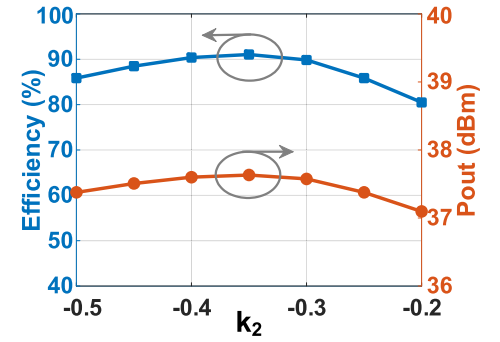

(a)

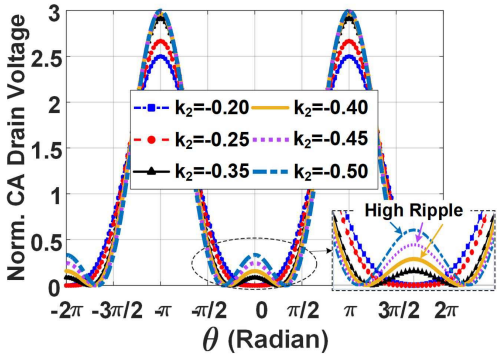

(b)

Fig. 3. CA performance tradeoff with different values of k_2. (a) Theoretical efficiency and output power. (b) Drain voltage with and without high ripples at the minima.

supply voltages, the BA fundamental design space expansion is only dominated by the parameter σ, which is actually determined by the input driving threshold, β_{bo}, at OBO.

While β_{bo} and k_2 are relatively independent of each other, when selecting different settings of β_{bo} and k_2, the power scale between peak power level and OBO level, defined as OBO_{dB} dB, would vary. Case studies under different scenarios are conducted to investigate the impact on the entire performance in terms of efficiency, output power, and design space of BA fundamental impedance.

At peak power level when $\beta = 1$, the output power from two BA cells in the peaking branch can be calculated as

$$P_{\text{ba,peak}} = i_{\text{ba,peak}}[1]^2 \cdot \text{Re}\left[Z_{\text{ba,pt,1st}}\right] \tag{16}$$

where $\text{Re}\left[Z_{\text{ba,pt,1st}}\right]$ is the real part of BA fundamental port impedance. Therefore, the OBO level of the proposed SLMBA can be calculated as

$$\text{OBO} \cdot P_{\text{obo}} = P_{\text{ca,sat}} + P_{\text{ba,peak}}. \tag{17}$$

1) Case I (Varying OBO and Peak Power Value for Different k_2): As shown in Fig. 4(a), when the entire SLMBA hits peak power level with $\beta = 1$, BA port impedance $Z_{\text{ba,pt,1st}}$ at the coupler port plane is expanded in the constant resistance contour, which is similar to Class-B/J or continuous Class-F fundamental impedance design continuum. According to Fig. 3, with constant value of β_{bo}, CA has different saturation output $P_{\text{ca,sat}}$ power for k_2 over $[-0.35, -0.20]$. This leads to the slight variation in output power value at OBO level and peak power level. Fig. 4(c) shows different OBO values and first peak efficiencies with constant input driving level ($\beta_{\text{bo}} = 0.5$) at OBO.

2) Case II (Constant OBO and Peak Power Value for Different k_2): To ensure constant OBO and peak power value with different k_2, the value of input driving threshold β_{bo} needs to be varied as well. According to (13) and (15), the BA fundamental port impedance can be expanded not only reactively but also resistively in the Smith chart, as shown in Fig. 4(b). Fig. 4(d) shows different β_{bo} values and first peak efficiencies with constant OBO level.

Given the expanded BA fundamental port design spaces from the above two cases, it is worth mentioning that such extended harmonic-to-fundamental control still follows the mechanism that the variation in CA second-harmonic impedance $Z_{\text{ca,2nd}}$ manipulates the fundamental port impedance $Z_{\text{ba,pt,1st}}$. The second-harmonic impedance $Z_{\text{ba,pt,2nd}}$ at BA ports needs to be properly controlled to achieve optimal peak power level performance in terms of efficiency and output power. As the BA fundamental port impedance naturally tracks the design space of the Class-B/J operation mode, the second-harmonic impedance at BA port $Z_{\text{ba,pt,2nd}}$ should be properly tuned following the Class-J theory such that:

$$Z_{\text{ba,pt,2nd}} = -j \cdot \frac{3\pi}{8}\delta, |\delta| \le \delta_{\max} \tag{18}$$

where $\delta_{\max}$ is the CM design space parameter that controls the second-harmonic design of Class-J BA. By substituting (13) and (15) to (18), $\delta_{\max}$ can be calculated and expressed as

$$\begin{aligned}\delta_{\max} &= \frac{\left|\frac{\sqrt{2}}{3\pi} \cdot \frac{1}{\sigma} \cdot \frac{I_{\max,\text{ca}}}{I_{\max,\text{ba}}}\right|}{1 + \sqrt{2}\left(\frac{1}{2} - \frac{8}{9\pi^2}\right) \cdot \frac{1}{\sigma} \cdot \frac{I_{\max,\text{ca}}}{I_{\max,\text{ba}}}} \\ &= \frac{1}{\frac{3\pi}{\sqrt{2}} \cdot \frac{(2\theta_b + \sin 2\theta_b) - 4\beta_{\text{bo}} \sin\theta_b}{2\pi(1-\beta_{\text{bo}})} \frac{I_{\max,\text{ba}}}{I_{\max,\text{ca}}} + \left(\frac{3\pi}{2} - \frac{8}{3\pi}\right)}.\end{aligned} \tag{19}$$

From the above analysis we can see, the design space for CA and BA can be extended while maintaining the good performance in terms of efficiency and output power.

III. Design of the Proposed Broadband SLMBA

To validate the proposed theory, an RF-input SLMBA was designed and fabricated using commercial gallium nitride (GaN) HEMTs (CG2H40010F) from Wolfspeed. The target frequency range is from 2.05 to 3.65 GHz to cover the 5G NR bands, e.g., N22 of 3410–3590 MHz, N40 of 2300–2400 MHz, and N41 of 2496–2690 MHz for cellular communication systems. Similar to the reported SLMBA configurations [33], [35], the input driving threshold $\beta_{\text{bo}} = 0.5$ was used and the target 8-dB OBO level was set for the design. While using the same CG2H40010F transistor for both CA and BA, larger drain supply voltage was used to achieve the required output power for the BA cell. The designed SLMBA was realized on a 31-mil-thick Taconic TLY-5 substrate with 2.2 dielectric constant. The schematic of the proposed SLMBA is shown in Fig. 5.

A broadband coupler was designed for both the input and output sections of the proposed SLMBA. The coupler was

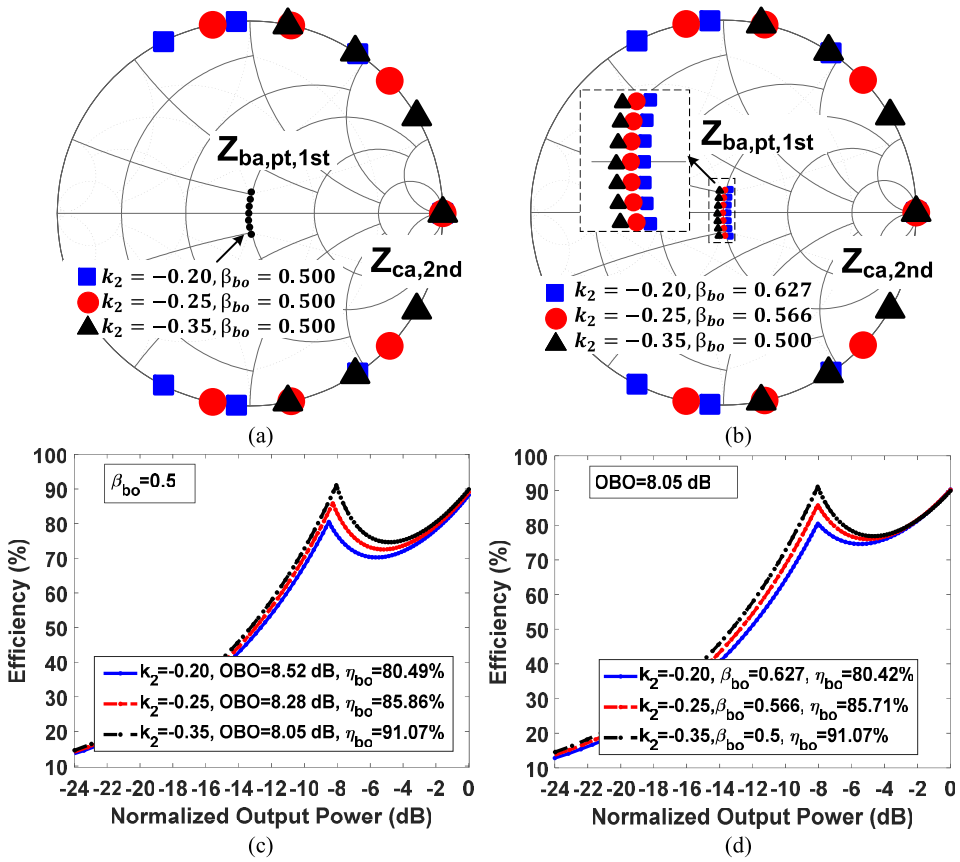

Fig. 4. Design space for BA port impedance under $Z_{ca,2nd}$ variation with different k_2 values. (a) Constant β_{bo}. (b) Varying β_{bo}; theoretical efficiency versus different values of k_2. (c) Varying OBO with constant β_{bo}. (d) Constant OBO with varying β_{bo}.

implemented using a three-section branch-line hybrid structure to cover the target bandwidth over 2.05–3.65 GHz, with the characteristic impedance of 50 Ω. The parameters of coupler are shown in Fig. 5.

According to the theoretical analysis of the proposed SLMBA in Section II, the value of design parameter k_2 was chosen within $[-0.35, -0.20]$, which can expand the fundamental load design space resistively and enlarge the second-harmonic load tuning range, while avoiding the overshooting behavior at the peaks and the high ripples at the minima for the drain voltage waveform.

A CG2H40010F transistor was used as the active device for CA with a drain supply of 20 V. Co-design of the CA OMN and coupler was required because the port impedance of the designed coupler cannot be maintained constant 50 Ω over such a wide bandwidth of 2.0–3.65 GHz. As shown in Fig. 6(a), the output port of OMN is connected to port 3 of the designed coupler. The parasitic and package parameters in commercial transistors usually limit the access to the device intrinsic plane. To extract the intrinsic drain current and voltage and intrinsic impedance, the de-embedded network for CG2H40010F transistor was used in the practical OMN design [40], [50], [51]. The topology and parameters of the CA OMN are shown in Fig. 5. During the design, both manual tuning and algorithm optimization were used for obtaining the good performance. The intrinsic CA load impedance trajectory is shown in Fig. 6(b), which follows the theoretical design space presented in Section II. Typically, the fundamental impedance has large value at low-frequency points, and vice versa at high-frequency points.

The IMN was also designed according to the source impedance extracted from the load–pull simulation. A 100-pF capacitor was used for DC blocking. A 10-Ω resistor is added to the gate bias line and ensure the stability of the transistor.

Two CG2H40010F transistors were also used as the active devices for the realization of the BA cells. In this case, the drain supply was set to 36 V. To simplify the design, we considered the BA impedance at saturation. The topology and parameters of BA OMN are shown in Fig. 5. It transformed the BA port impedance $Z_{ba,pt,1st}$ (when $\beta = 1$) to BA transistor intrinsic impedance $Z_{ba,1st}$ at saturation when the BA load modulation trajectory was on the real axis. The de-embedded network was also used for the BA OMN design so that intrinsic BA load impedance trajectory can be achieved, as shown in Fig. 7.

Similar to the design process in [32], [33], [34], and [38], a practical TL based phase shift network was designed to mimic the optimal phase shift value at each frequency point over the entire bandwidth of 2.05–3.65 GHz. The two-section equal ratio power divider (PD) was also designed and included in the schematic, as shown in Fig. 5.

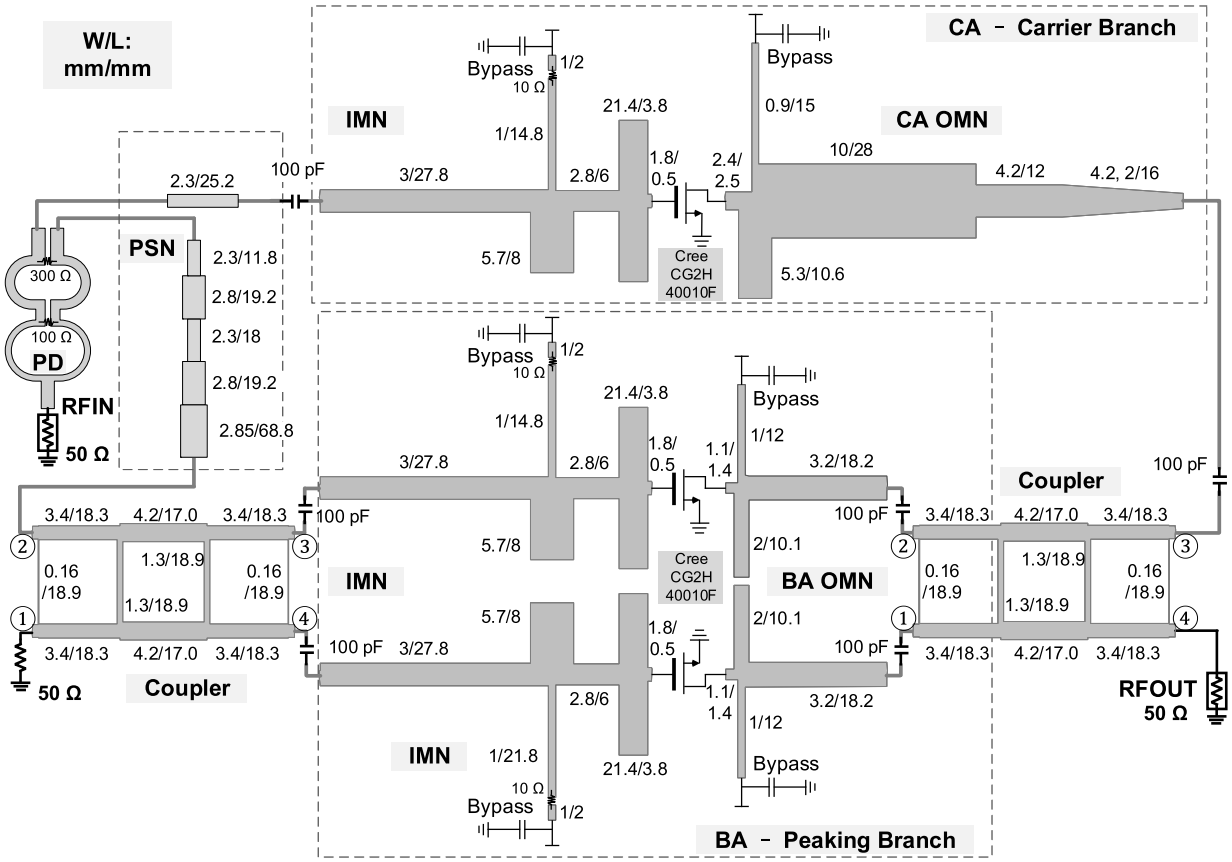

Fig. 5. Schematic of the proposed SLMBA.

Fig. 8 shows the simulated drain efficiency (DE) and gain of the proposed SLMBA versus the output power from 2.05 to 3.65 GHz with 0.2 GHz per step. The simulated results show a peak DE of 65.3%–75.8% with a saturated output power of 45.72–47.0 dBm. The back-off DE of 55.7%–62.1% and 53.1%–69.1% is achieved 6- and 8-dB OBO. A 9.6–12.0-dB gain was obtained at around 28-dBm output power level. Fig. 9 shows the simulated power-added efficiency (PAE) of 53.2%–64.5%, 47.4%–60.7%, and 49.0%–62.3% at saturation, 6-, and 8-dB OBO power level, respectively. Moreover, the simulated intrinsic BA fundamental load modulation trajectories at selected frequency points are plotted in Fig. 10, which is in good consistency with the theoretical design space continuum shown in Fig. 4(a) at saturation power level.

IV. Experimental Results

Fig. 11 presents the photograph of the fabricated SLMBA. The board is in a size of 22.25 cm × 12.8 cm. The drain supply voltage of 20 V and quiescent current of 30 mA for the carrier CA were set during all the measurements. The drain voltage of the peaking BA was set to 36 V to ensure good linearity, and the peaking bias voltage was set to −5.2 V. During the measurements, the CW and modulated signals were generated by a vector signal generator, and the output power was measured with a spectrum analyzer. A broadband linear driver amplifier was used to drive the SLMBA with enough input power. A broadband circulator was added between the driver and SLMBA to improve isolation.

A. Measurements With CW Signal

The SLMBA was first measured under CW signal stimulation at different operation frequencies with different input power levels. Fig. 12 presents the measured DE and gain versus output power at different operation frequencies. It can be seen that the Doherty-like behavior was achieved by the implemented SLMBA within the desired frequency band. Fig. 13 is the measured PAE versus output power at different operation frequencies. To better present broadband performance, the measured DE at different output power levels and output power at saturation versus the operation frequency are presented in Fig. 14. Over the realized bandwidth, the proposed SLMBA achieves a measured DE of 50.5%–66.2% at 8-dB OBO, 51.2%–65.8% at 6-dB OBO, and 61.2%–79.7% at peak power, with output power from 45.2 to 46.8 dBm.

The measured PAE and the gain at different output power levels over the bandwidth are also plotted in Fig. 15 with a measured PAE of 40.5%–57.7% at 8-dB OBO, 40.0%–56.3% at 6-dB OBO, and 43.5%–62.2% at peak power level, respectively. A 7.8–10.8-dB gain was obtained at around 28-dBm output power level. It should be noted that the transducer power gain of this SLMBA prototype is relatively low, i.e., 4.9–7.1-dB at peak output power. This leads the PAE to be much lower than DE reported above. To directly use this

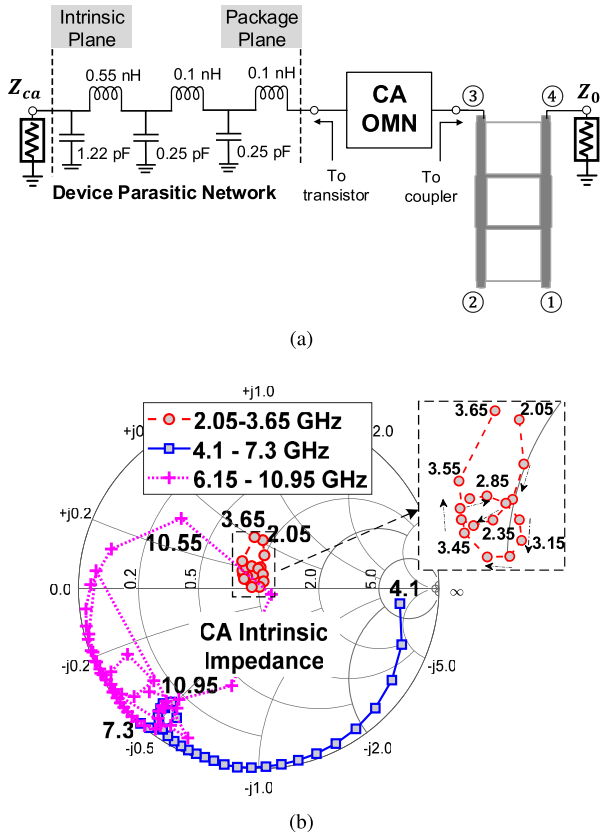

Fig. 6. (a) CA OMN: Co-design with output quadrature coupler. (b) Design impedance of the CA load matching network on the Smith chart with reference impedance 40 Ω.

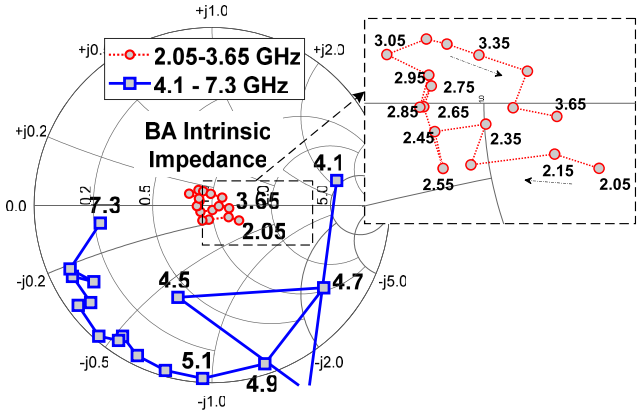

Fig. 7. Design impedance of the BA load matching network on the Smith chart with reference impedance 50 Ω.

PA prototype in a real system, a large driver amplifier would be required to keep the system efficiency [39]. Besides the tradeoff in gain *versus* frequency *versus* bandwidth [40], the low gain is a general issue for the SLMBA-based architectures [33], [34], [37], [38], [39]. At least half of the input power is steered to drive large peaking BA and wasted at OBO level. This leads to the low gain for the carrier CA and also insufficient gain for peaking BA. This issue needs to be addressed in future research.

Compared with the simulation results presented in Figs. 8 and 9, the measured results slightly deviated from the simulation results. This can be attributed to fabrication

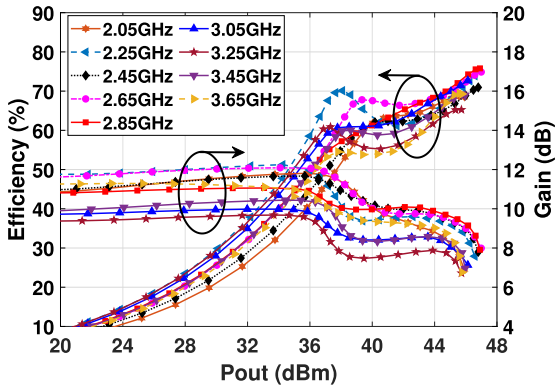

Fig. 8. Simulated DE and gain versus output power over 2.05–3.65 GHz.

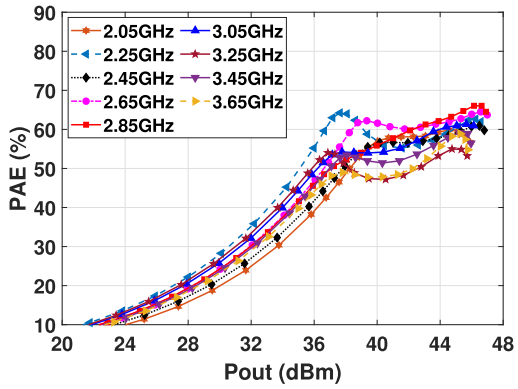

Fig. 9. Simulated PAE versus output power over 2.05–3.65 GHz.

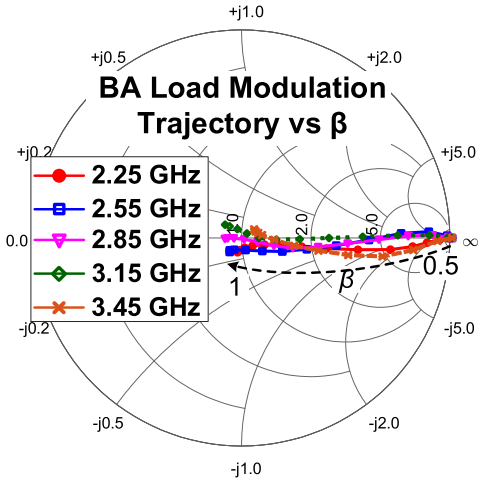

Fig. 10. BA load modulation trajectories versus β.

tolerances of the prototype board and inaccuracy of the large-signal model of the device in deep Class-C bias [31].

B. Measurements With Modulated Signal

1) Single-Band Measurements: To evaluate the linearity and efficiency performance under modulated signals' stimulation, 60- and 100-MHz LTE signals with 8-dB peak-to-average-power ratio (PAPR) were used to test the SLMBA from 2.05 to 3.65 GHz.

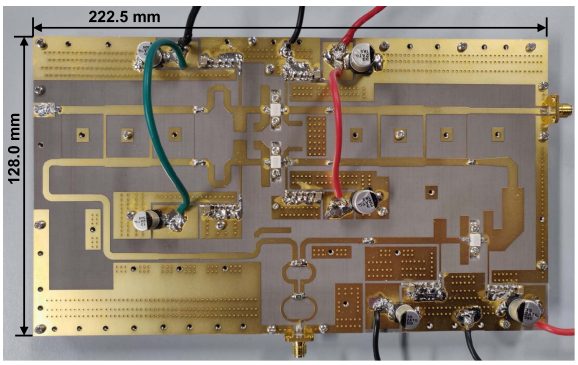

Fig. 11. Photograph of the fabricated SLMBA.

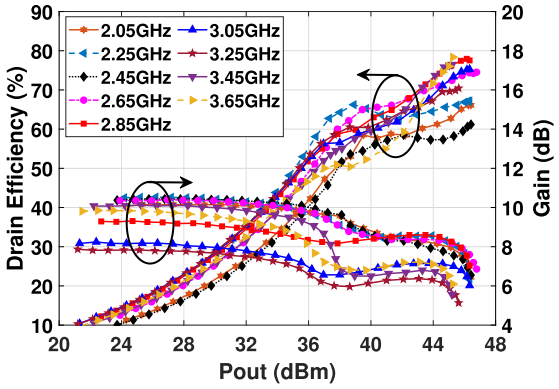

Fig. 12. Measured DE and gain versus output power over 2.05–3.65 GHz.

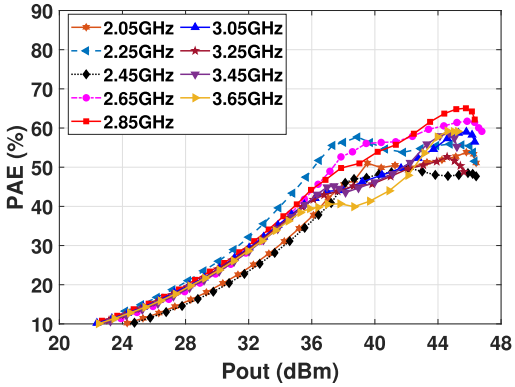

Fig. 13. Measured PAE versus output power over 2.05–3.65 GHz.

To linearize the PA, the magnitude-selective affine (MSA) function-based digital predistortion (DPD) model [52] was used. When tested with the 60-MHz LTE signal, the memory length $M = 20$ and the number of thresholds $K = 7$ were used. While under the 100-MHz LTE signal, $M = 22$ and $K = 10$.

Fig. 16(a), (c), and (e) presents the output spectrum with and without DPD linearization under the stimulation of the 60-MHz signal at 2.25, 2.75, and 3.25 GHz, respectively. The measured adjacent channel power ratios (ACPRs) of the SLMBA were −23.1/−23.7 dBc at 2.25 GHz, −24.6/−23.8 dBc at 2.75 GHz, and −23.2/−22.3 dBc at 3.25 GHz without DPD. After DPD correction, the

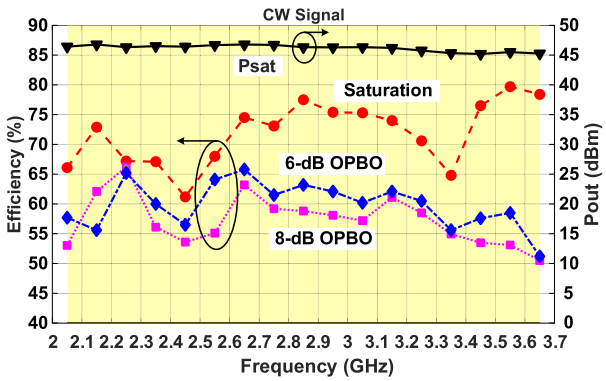

Fig. 14. Measured DE and output power versus frequency with CW signal.

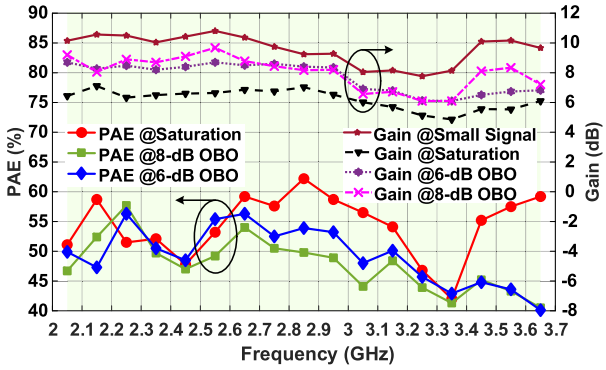

Fig. 15. Measured PAE and gain versus frequency with CW signal.

ACPRs were improved to −53.4/−53.7 dBc at 2.25 GHz, −53.3/−52.6 dBc at 2.75 GHz, and −53.1/−52.3 dBc at 3.25 GHz. The average output power of around 37.6 dBm was achieved at these three frequencies after DPD correction, with average DE of 64.7%, 61.8%, and 59.8%, respectively. The AM–AM and AM–PM characteristics with and without DPD are given in Fig. 16(b), (d), and (f).

Under the 100-MHz LTE signal stimulation, the measured ACPRs were −22.9/−23.3 dBc at 2.25 GHz, −24.2/−23.0 dBc at 2.75 GHz, and −22.5/−21.4 dBc at 3.25 GHz, as shown in Fig. 17(a), (c), and (e). After applying DPD, the ACPRs were improved to −47.7/−47.8 dBc at 2.25 GHz, −48.0/−47.4 dBc at 2.75 GHz, and −48.9/−47.7 dBc at 3.25 GHz, respectively. Around 37.9-, 38.2-, and 37.0-dBm average output power was achieved at these three frequencies after DPD, with average DE of 63.5%, 61.7%, and 61.1%, respectively. The AM–AM and AM–PM characteristics with and without DPD are also shown here in Fig. 17(b), (d), and (f).

In Fig. 18, we summarize the measured average DE, output power, and ACPR performance from 2.05 to 3.65 GHz under the 60-MHz LTE signal stimulation. About 50.7%–64.7% average DE was achieved by the fabricated SLMBA prototype with average output power of 36.2–38.5-dBm. ACPR was improved to better than −45.2 dBc after applying DPD. In addition, Fig. 19 summarizes the measured average DE, output power, and ACPR performance from 2.05 to 3.65 GHz under the 100-MHz LTE signal stimulation.

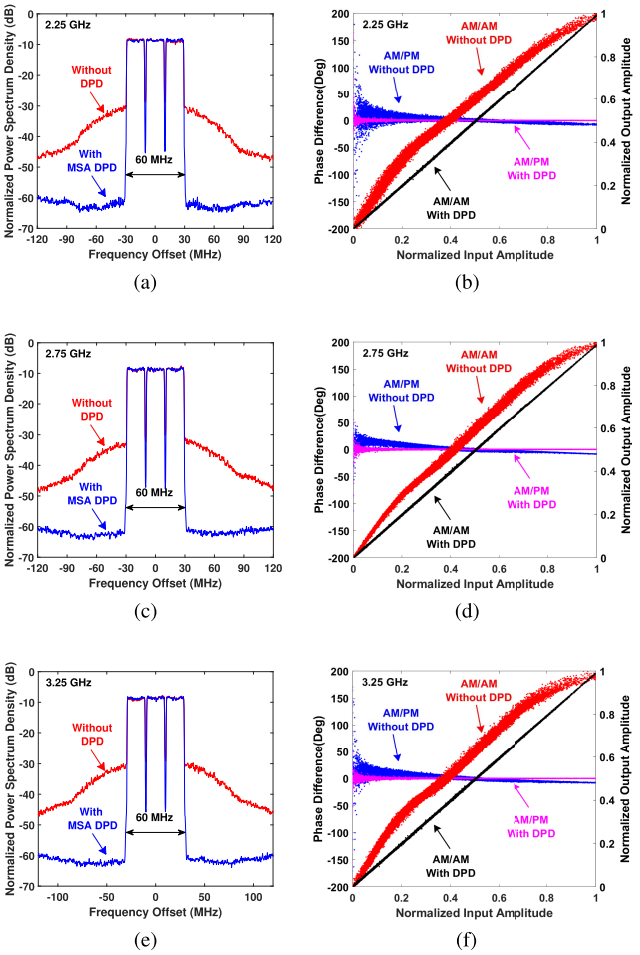

Fig. 16. Modulated signal measurement results of the proposed SLMBA with and without DPD-model corrections under 60-MHz LTE signal. Output spectrum at (a) 2.25, (c) 2.75, and (e) 3.25 GHz. AM–AM and AM–PM at (b) 2.25, (d) 2.75, and (f) 3.25 GHz.

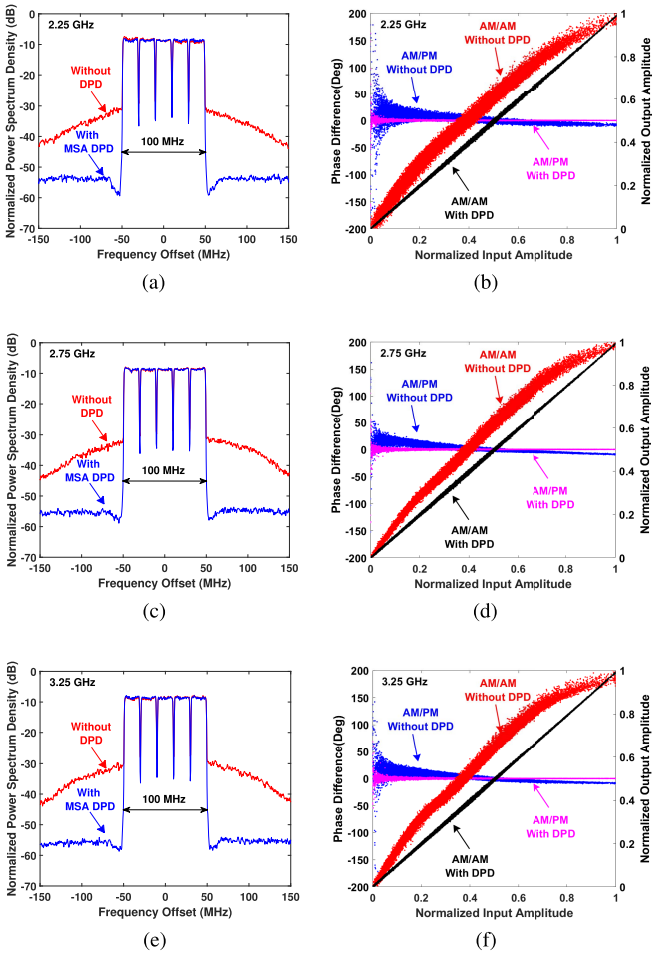

Fig. 17. Modulated signal measurement results of the proposed SLMBA with and without DPD linearization under 100-MHz LTE signal. Output spectrum at (a) 2.25, (c) 2.75, and (e) 3.25 GHz. AM–AM and AM–PM at (b) 2.25, (d) 2.75, and (f) 3.25 GHz.

Over 2.05–3.65 GHz, the prototype achieves 49.0%–63.5% average DE, average output power of 36.1–38.3-dBm, and −40.3∼−49.2-dBc ACPR after DPD correction.

2) Concurrent Dual-Band Measurements: The proposed SLMBA was also measured under concurrent dual-band signal stimulation. Concurrent dual-band modulated signal with 7-dB PAPR was used with 20-MHz signal bandwidth at each band. To validate the performance under different scenarios, the PA was measured under different carrier frequencies with different frequency spacing between the bands. During the measurement, the average output power of the two frequency bands was kept almost equal. Dual-band memory polynomial (MP) model-based DPD was performed to linearize the proposed SLMBA under concurrent operation [53].

a) Frequency spacing of 500 MHz: In this scenario, the center frequencies of the two signals were 2.15 and 2.65 GHz for LTE B1 and B7 bands, respectively. Fig. 20 represents the corresponding output spectrum. The average efficiency of 54.6% was achieved with around 35.5 dBm average output power at each band. The ACPRs were −29.5 and −27.9 dBc without DPD correction and improved to −48.1 and −46.9 dBc with DPD, at 2.15 and 2.65 GHz, respectively.

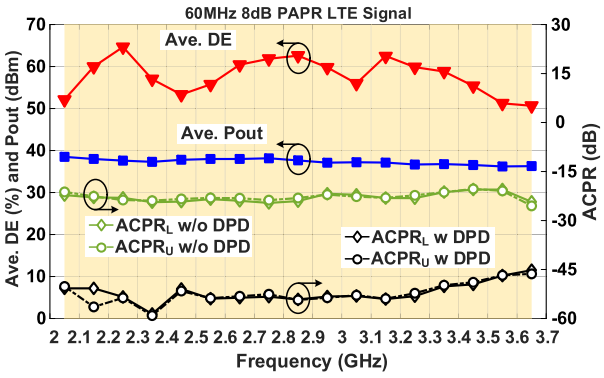

Fig. 18. Measured average DE, output power, and ACPR versus frequency under the 60-MHz 8-dB PAPR LTE signal test over 2.05–3.65 GHz.

b) Frequency spacing of 1000 MHz: In this scenario, the center frequencies of the two signals are 2.55 and 3.55 GHz corresponding to 5G NR N7 and N48 bands, respectively. Fig. 21 represents the corresponding output spectrum. The average efficiency of 45.4% was achieved with around 34.2 dBm average output power at each band. The ACPRs

TABLE I
PERFORMANCE COMPARISON OF RECENTLY PUBLISHED LOAD MODULATED PAS

Ref. (Year)	Technique N/A	Freq. /FBW. GHz/%	P_{max} (dBm)	Gain (dB)	OBO (dB)	DE @OBO (%)	DE @Pmax (%)	Signal BW (MHz)	PAPR (dB)	P_{ave} (dBm)	DE @ave (%)	ACPR (dBc)
[30] 2017	RF-Input LMBA	1.8-3.8 /71	42-44	11-12	6	33-49	46-70	3.84	9	31-32.1*	17-26* $^{\Psi}$	-26.6∼-30* $^{\#}$
[29] 2018	Dual-Input LMBA	1.7-2.5 /38.1	48-48.9	9.9-13.2	6/8	43-53$^{\Psi}$/39-50$^{\Psi}$	48-58*	20	9	39	40$^{\Psi}$	-49
[33] 2020	RF-Input SLMBA	3.05-3.55 /15.2	42.3-43.7	9.5-10.3	6/8/10	50.9-64.9/46.8-60.7/43.2-51.4	60.8-74.8	40/80/200	6/8/10	33.5/33.8/33	57.8/49.9/48.2	-46.7/-45.2/-43.9
[34] 2020	RF-Input PD-LMBA	1.5-2.7 /57	43	8	6/10	47-61/47-58	58-72	10	9.5	33.5	47-58	-25.8$^{\#}$
[38] 2020	RF-input PD-ALMBA	0.55-2.2 /120	41-43	8.0-15.0	6/10	40-60/39-64	49-82	20	10	33	51-62	-28$^{\#}$
[32] 2020	RF-Input CM-LMBA	1.45-2.45 /51.3	45.6-46.7	11.2-13.4	6/8	51.2-64.4/47.8-55.7	67.1-77.9	100	8	37.5-38.2	40-48.6$^{\Psi}$	-44.3∼-49.0
[37] 2021	RF-Input H-ALMBA	1.7-3.0 /55	42-43	13-8	6/10	50-61*/50-66	63-81	20	10	32	50-56	-27$^{\#}$
[35] 2022	RF-input W-SLMBA	1.80-2.75 /41.8	44.6-45.8	9.4-11.7	6/8	51.0-63.8/51.8-69.0	60.2-68.3	60/100	8	36.0-38.3/35.9-38.2	51.2-58.4/50.2-59.1	-45.4∼-54.8/-45.1∼-51.5
This work	RF-input SLMBA	2.05-3.65 /56.1	45.2-46.8	7.8-10.8	6/8	51.2-65.8/50.5-66.2	61.2-79.7	60/100	8	36.2-38.5/36.1-38.3	50.7-64.7/49.0-63.5	-45.2∼-59.1/-40.3∼-49.2

*Graphically estimated, $^{\Psi}$Power added efficiency (PAE), $^{\#}$ACPR without DPD.

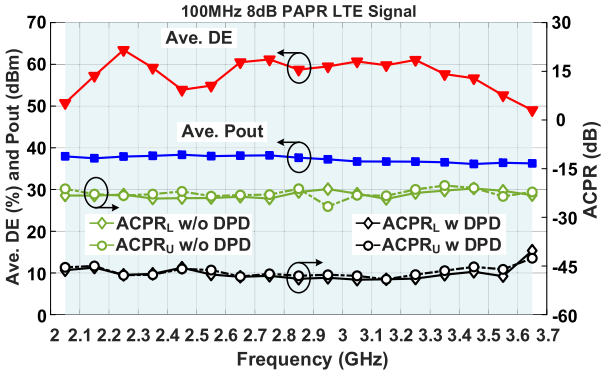

Fig. 19. Measured average DE, output power, and ACPR versus frequency under the 100-MHz 8-dB PAPR LTE signal test 2.05–3.65 GHz.

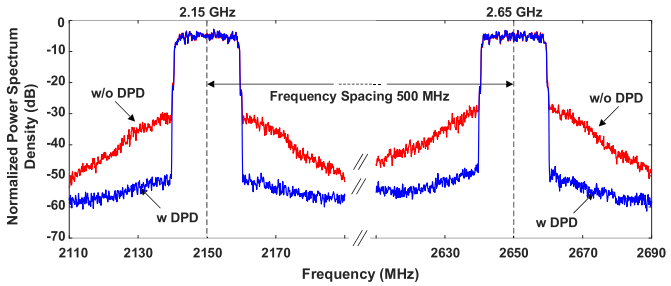

Fig. 20. Output spectrum at 2.15 and 2.65 GHz with and without DPD linearization under concurrent dual-band signal stimulation with a 500-MHz frequency spacing.

were −24.3 and −26.8 dBc without DPD correction and improved to −46.6 and −46.8 dBc with DPD, at 2.55 and 3.55 GHz, respectively.

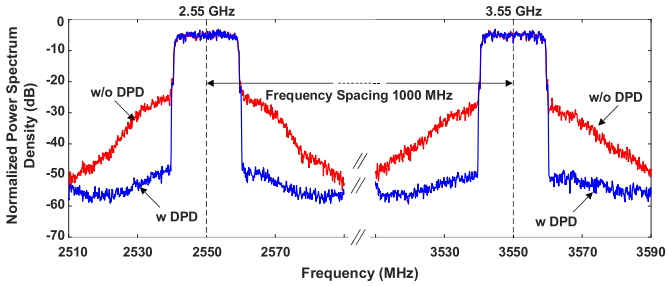

Fig. 21. Output spectrum at 2.55 and 3.55 GHz with and without DPD linearization under concurrent dual-band signal stimulation with a 1000-MHz frequency spacing.

c) Frequency spacing of 1300 MHz: In this scenario, the center frequencies of the two signals are 2.15 and 3.45 GHz, corresponding to 5G NR N1 and N48 bands, respectively. Fig. 22 represents the corresponding output spectrum. The average efficiency of 45.2% was achieved with around 32.8 dBm average output power at each band. The ACPRs were −25.8 and −25.9 dBc without DPD correction and improved to −47.5 and −47.5 dBc with DPD, at 2.15 and 3.45 GHz, respectively.

Although the main target of this design was focused on continuous bandwidth extension, the above measurements show that the proposed SLMBA can also support concurrent operation with different frequency distributions and large frequency spacing. The proposed SLMBA presents promising performance in terms of efficiency, output power, and linearity, at the concurrent dual-band scenario with various frequency spacing.

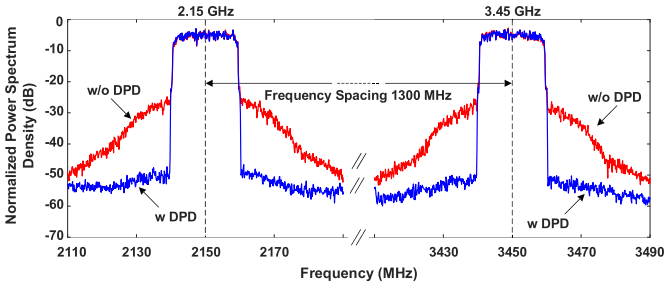

Fig. 22. Output spectrum at 2.15 and 3.45 GHz with and without DPD linearization under concurrent dual-band signal stimulation with a 1300-MHz frequency spacing.

C. Performance Comparison

Table I summarizes the performance of some recently reported LMBA and SLMBA-based configurations. Compared with other published work, the proposed SLMBA shows excellent efficiency performance at both saturation and 6/8-dB OBO levels. Particularly, it achieves 56.1% fractional bandwidth over 2.05–3.65 GHz. Compared with W-SLMBA reported in [35], the proposed SLMBA design approach enables significant improvement in fractional bandwidth (improved approximately by 34%), without adding extra complexity. Furthermore, the proposed SLMBA achieves good average efficiency under both the single-band and concurrent dual-band scenarios, proving that it can be a good candidate for the 5G NR band, e.g., N7, N22, and N40 bands.

V. Conclusion

An RF-input broadband SLMBA is proposed with extended high-efficiency design space, via proper manipulation of CA second-harmonic load impedance over an expanded range. The enlarged CA load design space not only can provide the time-domain-varying drain current waveform over the design continuum, but also allows maintaining high OBO efficiency over an extended operation bandwidth. To validate the theory, a broadband SLMBA operating at 2.05–3.65 GHz was designed following the proposed design methodology and fabricated using packaged devices. The implemented SLMBA achieves a measured DE of 61.2%–79.7% at saturation and 50.5%–66.2% at 8-dB OBO.

References

[1] *Base Station (BS) Radio Transmission and Reception, 3rd Generation Partnership Project (3GPP), Technical Specification (TS)* document 38.104, Version 16.6.0., Jan. 2021.

[2] Qualcomm Technologies. (2017). *Spectrum for 4G and 5G*. [Online]. Available: https://www.qualcomm.com/media/documents/files/spectrum-for-4g-and-5g.pdf

[3] J. Pang, Z. Dai, Y. Li, M. Li, and A. Zhu, "Multiband dual-mode Doherty power amplifier employing phase periodic matching network and reciprocal gate bias for 5G applications," *IEEE Trans. Microw. Theory Techn.*, vol. 68, no. 6, pp. 2382–2397, Jun. 2020.

[4] J. Pang, S. He, C. Huang, Z. Dai, J. Peng, and F. You, "A post-matching Doherty power amplifier employing low-order impedance inverters for broadband applications," *IEEE Trans. Microw. Theory Techn.*, vol. 63, no. 12, pp. 4061–4071, Dec. 2015.

[5] X. Y. Zhou, S. Y. Zheng, W. S. Chan, X. Fang, and D. Ho, "Postmatching Doherty power amplifier with extended back-off range based on self-generated harmonic injection," *IEEE Trans. Microw. Theory Techn.*, vol. 66, no. 4, pp. 1951–1963, Apr. 2018.

[6] J. Xia, M. Yang, Y. Guo, and A. Zhu, "A broadband high-efficiency Doherty power amplifier with integrated compensating reactance," *IEEE Trans. Microw. Theory Techn.*, vol. 64, no. 7, pp. 2014–2024, Jul. 2016.

[7] X. H. Fang and K.-M. M. Cheng, "Extension of high-efficiency range of Doherty amplifier by using complex combining load," *IEEE Trans. Microw. Theory Techn.*, vol. 62, no. 9, pp. 2038–2047, Sep. 2014.

[8] R. Darraji, D. Bhaskar, T. Sharma, M. Helaoui, P. Mousavi, and F. M. Ghannouchi, "Generalized theory and design methodology of wideband Doherty amplifiers applied to the realization of an octave-bandwidth prototype," *IEEE Trans. Microw. Theory Techn.*, vol. 65, no. 8, pp. 3014–3023, Aug. 2017.

[9] N. S. Mannem, T.-Y. Huang, and H. Wang, "Broadband active load-modulation power amplification using coupled-line baluns: A multifrequency role-exchange coupler Doherty amplifier architecture," *IEEE J. Solid-State Circuits*, vol. 56, no. 10, pp. 3109–3122, Oct. 2021.

[10] P. Colantonio, F. Giannini, G. Leuzzi, and E. Limiti, "High efficiency low-voltage power amplifier design by second-harmonic manipulation," *Int. J. RF Microw. Comput.-Aided Eng.*, vol. 10, no. 1, pp. 19–32, Jan. 2000.

[11] P. Wright, J. Lees, J. Benedikt, P. J. Tasker, and S. C. Cripps, "A methodology for realizing high efficiency class-J in a linear and broadband PA," *IEEE Trans. Microw. Theory Techn.*, vol. 57, no. 12, pp. 3196–3204, Dec. 2009.

[12] S. C. Cripps, P. J. Tasker, A. L. Clarke, J. Lees, and J. Benedikt, "On the continuity of high efficiency modes in linear RF power amplifiers," *IEEE Microw. Wireless Compon. Lett.*, vol. 19, no. 10, pp. 665–667, Oct. 2009.

[13] V. Carrubba et al., "On the extension of the continuous class-F mode power amplifier," *IEEE Trans. Microw. Theory Techn.*, vol. 59, no. 5, pp. 1294–1303, May 2011.

[14] N. Tuffy, L. Guan, A. Zhu, and T. J. Brazil, "A simplified broadband design methodology for linearized high-efficiency continuous class-F power amplifiers," *IEEE Trans. Microw. Theory Techn.*, vol. 60, no. 6, pp. 1952–1963, Jun. 2012.

[15] T. Sharma, R. Darraji, P. Mousavi, and F. M. Ghannouchi, "Generalized design of continuous-mode second harmonic tuned amplifiers," *Microw. Opt. Technol. Lett.*, vol. 58, pp. 2787–2789, Sep. 2016.

[16] Z. Yang et al., "Bandwidth extension of Doherty power amplifier using complex combining load with noninfinity peaking impedance," *IEEE Trans. Microw. Theory Techn.*, vol. 67, no. 2, pp. 765–777, Feb. 2019.

[17] T.-W. Li, M.-Y. Huang, and H. Wang, "Millimeter-wave continuous-mode power amplifier for 5G MIMO applications," *IEEE Trans. Microw. Theory Techn.*, vol. 67, no. 7, pp. 3088–3098, Jul. 2019.

[18] S. K. Dhar et al., "Investigation of input–output waveform engineered continuous inverse class-F power amplifiers," *IEEE Trans. Microw. Theory Techn.*, vol. 67, no. 9, pp. 3547–3561, Sep. 2019.

[19] S. K. Dhar et al., "Input-harmonic-controlled broadband continuous class-F power amplifiers for sub-6-GHz 5G applications," *IEEE Trans. Microw. Theory Techn.*, vol. 68, no. 7, pp. 3120–3133, Jul. 2020.

[20] X. Chen, W. Chen, F. M. Ghannouchi, Z. Feng, and Y. Liu, "A broadband Doherty power amplifier based on continuous-mode technology," *IEEE Trans. Microw. Theory Techn.*, vol. 64, no. 12, pp. 4505–4517, Dec. 2016.

[21] W. Shi et al., "Broadband continuous-mode Doherty power amplifiers with noninfinity peaking impedance," *IEEE Trans. Microw. Theory Techn.*, vol. 66, no. 2, pp. 1034–1046, Feb. 2018.

[22] D. Gan and W. Shi, "Design of a broadband Doherty power amplifier based on hybrid continuous mode," *IEEE Access*, vol. 7, pp. 86194–86204, 2019.

[23] G. Naah and R. Giofre, "Empowering the bandwidth of continuous-mode symmetrical Doherty amplifiers by leveraging on fuzzy logic techniques," *IEEE Trans. Microw. Theory Techn.*, vol. 68, no. 7, pp. 3134–3147, Jul. 2020.

[24] W. Shi et al., "Design and analysis of continuous-mode Doherty power amplifier with second harmonic control," *IEEE Trans. Circuits Syst. II, Exp. Briefs*, vol. 68, no. 7, pp. 2247–2251, Jul. 2021.

[25] J. Pang et al., "Broadband GaN MMIC Doherty power amplifier using continuous-mode combining for 5G sub-6 GHz applications," *IEEE J. Solid-State Circuits*, vol. 57, no. 7, pp. 2143–2154, Jul. 2022.

[26] D. J. Shepphard, J. Powell, and S. C. Cripps, "An efficient broadband reconfigurable power amplifier using active load modulation," *IEEE Microw. Wireless Compon. Lett.*, vol. 26, no. 6, pp. 443–445, Jun. 2016.

[27] D. J. Shepphard, J. Powell, and S. C. Cripps, "A broadband reconfigurable load modulated balanced amplifier (LMBA)," in *IEEE MTT-S Int. Microw. Symp. Dig.*, Jun. 2017, pp. 947–949.

[28] R. Quaglia and S. Cripps, "A load modulated balanced amplifier for telecom applications," *IEEE Trans. Microw. Theory Techn.*, vol. 66, no. 3, pp. 1328–1338, Mar. 2018.

[29] R. Quaglia, J. Powell, D. Shepphard, P. Tasker, and S. Cripps, "Analysis and characterization of a load modulated balanced amplifier for base-station applications," in *Proc. 11th German Microw. Conf. (GeMiC)*, Mar. 2018, pp. 1–4.

[30] P. H. Pednekar, E. Berry, and T. W. Barton, "RF-input load modulated balanced amplifier with octave bandwidth," *IEEE Trans. Microw. Theory Techn.*, vol. 65, no. 12, pp. 5181–5191, Dec. 2017.

[31] P. H. Pednekar, W. Hallberg, C. Fager, and T. W. Barton, "Analysis and design of a Doherty-like RF-input load modulated balanced amplifier," *IEEE Trans. Microw. Theory Techn.*, vol. 66, no. 12, pp. 5322–5335, Dec. 2018.

[32] J. Pang, C. Chu, Y. Li, and A. Zhu, "Broadband RF-input continuous-mode load-modulated balanced power amplifier with input phase adjustment," *IEEE Trans. Microw. Theory Techn.*, vol. 68, no. 10, pp. 4466–4478, Oct. 2020.

[33] J. Pang et al., "Analysis and design of highly efficient wideband RF-input sequential load modulated balanced power amplifier," *IEEE Trans. Microw. Theory Techn.*, vol. 68, no. 5, pp. 1741–1753, May 2020.

[34] Y. Cao and K. Chen, "Pseudo-Doherty load-modulated balanced amplifier with wide bandwidth and extended power back-off range," *IEEE Trans. Microw. Theory Techn.*, vol. 68, no. 7, pp. 3172–3183, Jul. 2020.

[35] C. Chu et al., "Waveform engineered sequential load modulated balanced amplifier with continuous class-F^{-1} and class-J operation," *IEEE Trans. Microw. Theory Techn.*, vol. 70, no. 2, pp. 1269–1283, Feb. 2022.

[36] C. Chu, T. Sharma, S. K. Dhar, R. Darraji, and A. Zhu, "Investigation of input nonlinearity in sequential load modulated balanced amplifiers," in *IEEE MTT-S Int. Microw. Symp. Dig.*, Jun. 2022, pp. 414–417.

[37] Y. Cao, H. Lyu, and K. Chen, "Continuous-mode hybrid asymmetrical load-modulated balanced amplifier with three-way modulation and multi-band reconfigurability," *IEEE Trans. Circuits Syst. I, Reg. Papers Reg. Papers*, vol. 69, no. 3, pp. 1077–1090, Mar. 2022.

[38] Y. Cao, H. Lyu, and K. Chen, "Asymmetrical load modulated balanced amplifier with continuum of modulation ratio and dual-octave bandwidth," *IEEE Trans. Microw. Theory Techn.*, vol. 69, no. 1, pp. 682–696, Jan. 2021.

[39] P. Saad and R. Hou, "Symmetrical load modulated balanced power amplifier with asymmetrical output coupling for load modulation continuum," *IEEE Trans. Microw. Theory Techn.*, vol. 70, no. 4, pp. 2315–2327, Apr. 2022.

[40] P. Colantonio, F. Giannini, and E. Limiti, *High Efficiency RF and Microwave Solid State Power Amplifiers*. New York, NY, USA: Wiley, 2009.

[41] T. Sharma et al., "High-efficiency input and output harmonically engineered power amplifiers," *IEEE Trans. Microw. Theory Techn.*, vol. 66, no. 2, pp. 1002–1014, Feb. 2018.

[42] T. Sharma et al., "Simplified first-pass design of high-efficiency class-F^{-1} power amplifiers based on second-harmonic minima," *IEEE Trans. Microw. Theory Techn.*, vol. 67, no. 7, pp. 3147–3161, Jul. 2019.

[43] S. K. Dhar et al., "Modeling of input nonlinearity and waveform engineered high-efficiency class-F power amplifiers," *IEEE Trans. Microw. Theory Techn.*, vol. 68, no. 10, pp. 4216–4228, Oct. 2020.

[44] Z. Liu, T. Sharma, C. R. Chappidi, S. Venkatesh, Y. Yu, and K. Sengupta, "A 42–62 GHz transformer-based broadband mm-wave InP PA with second-harmonic waveform engineering and enhanced linearity," *IEEE Trans. Microw. Theory Techn.*, vol. 69, no. 1, pp. 756–773, Jan. 2021.

[45] C. Chu, T. Sharma, S. K. Dhar, R. Darraji, J. Pang, and A. Zhu, "Phase compensated sequential load modulated balanced amplifier using harmonically tuned control amplifier," in *Proc. 51st Eur. Microw. Conf. (EuMC)*, Apr. 2022, pp. 346–349.

[46] C. Chu, S. K. Dhar, T. Sharma, and A. Zhu, "Class-iF^{-1} : Linearity enhanced high efficiency power amplifier," in *Proc. IEEE Topical Conf. RF/Microwave Power Model. Radio Wireless Appl. (PAWR)*, Jan. 2022, pp. 39–41.

[47] T. Sharma, R. Darraji, and F. Ghannouchi, "A methodology for implementation of high-efficiency broadband power amplifiers with second-harmonic manipulation," *IEEE Trans. Circuits Syst. II, Exp. Briefs*, vol. 63, no. 1, pp. 54–58, Jan. 2016.

[48] M. Yang, J. Xia, Y. Guo, and A. Zhu, "Highly efficient broadband continuous inverse class-F power amplifier design using modified elliptic low-pass filtering matching network," *IEEE Trans. Microw. Theory Techn.*, vol. 64, no. 5, pp. 1515–1525, May 2016.

[49] J. H. Kim, S. J. Lee, B. H. Park, S. H. Jang, J. H. Jung, and C. S. Park, "Analysis of high-efficiency power amplifier using second harmonic manipulation: Inverse class-F/J amplifiers," *IEEE Trans. Microw. Theory Techn.*, vol. 59, no. 8, pp. 2024–2036, Aug. 2011.

[50] A. Raffo, F. Scappaviva, and G. Vannini, "A new approach to microwave power amplifier design based on the experimental characterization of the intrinsic electron-device load line," *IEEE Trans. Microw. Theory Techn.*, vol. 57, no. 7, pp. 1743–1752, Jul. 2009.

[51] H. Jang, P. Roblin, and Z. Xie, "Model-based nonlinear embedding for power-amplifier design," *IEEE Trans. Microw. Theory Techn.*, vol. 62, no. 9, pp. 1986–2002, Sep. 2014.

[52] Y. Li, W. Cao, and A. Zhu, "Instantaneous sample indexed magnitude-selective affine function-based behavioral model for digital predistortion of RF power amplifiers," *IEEE Trans. Microw. Theory Techn.*, vol. 66, no. 11, pp. 5000–5010, Nov. 2018.

[53] Y.-J. Liu, W. Chen, J. Zhou, B.-H. Zhou, and F. M. Ghannouchi, "Digital predistortion for concurrent dual-band transmitters using 2-D modified memory polynomials," *IEEE Trans. Microw. Theory Techn.*, vol. 61, no. 1, pp. 281–290, Jan. 2013.

Chenhao Chu (Member, IEEE) received the M.S. degree (Hons.) in electronic information engineering from The City University of Hong Kong (CityU), Hong Kong, China, in 2017. He is currently pursuing the Ph.D. degree in electronic engineering at University College Dublin (UCD), Dublin, Ireland.

From October 2017 to September 2018, he was a Research Assistant with the State Key Laboratory of Millimeter Waves, Department of Electronic Engineering, CityU. He is currently with the RF and Microwave Research Group, School of Electrical and Electronic Engineering, UCD. His research interests include broadband high-efficiency power amplifiers, MMIC power amplifier design for RF/mm-wave applications, and antenna-in-package (AiP) for phased arrays.

Mr. Chu won three prizes in IEEE Microwave Theory and Technology Society (MTT-S) High Efficiency Power Amplifier Student Design Competitions (HEPA-SDCs), i.e., 2nd place at the 2021 International Microwave Symposium (IMS2021), 1st place for both ACPR-FoM and EVM FoM at 2022 Radio and Wireless Week (RWW2022), and 3rd place at IMS2022. He was also on the Final List of Student Paper Competition at RWW2022 and Three-Minute Thesis Competition (3MT) at IMS2022. He was a recipient of the Best Student Paper Award (1st Place) of the 19th Royal Irish Academy/the International Union of Radio Science (RIA/URSI) Research Colloquium on Radio Science and Communications in October 2022. He is a Reviewer for journals, including IEEE TRANSACTIONS ON MICROWAVE THEORY AND TECHNIQUES, IEEE TRANSACTIONS ON CIRCUITS AND SYSTEMS—I: REGULAR PAPERS, and *IEEE Microwave Magazine*.

Jingzhou Pang (Senior Member, IEEE) received the B.S. degree in electrical engineering and the Ph.D. degree in circuits and systems from the University of Electronic Science and Technology of China (UESTC), Chengdu, China, in 2010 and 2016, respectively.

From December 2016 to July 2018, he was with Huawei Technologies Company Ltd., Chengdu, where he was an Engineer in charge of the research and development of 5G high-efficiency power amplifiers and transmitters. From July 2018 to August 2020, he was with the RF and Microwave Research Group, University College Dublin (UCD), Dublin, Ireland, where he was a Research Fellow in charge of the research of novel broadband transmitter architectures and radio frequency (RF)/microwave/mm-wave monolithic microwave integrated circuit (MMIC) power amplifiers. He is currently an Associate Professor with the School of Microelectronics and Communication Engineering, Chongqing University, Chongqing, China. His research interests include broadband high-efficiency power amplifier systems, bandwidth extension techniques for high-efficiency transmitters, and MMIC power amplifier design for RF/microwave and mm-wave applications.

Dr. Pang was a recipient of the EDGE Marie Sklodowska-Curie Individual Fellowship and the Third Place Award of the High Efficiency Power Amplifier Student Design Competition at the IEEE Microwave Theory and Techniques Society (IEEE MTT-S) International Microwave Symposium (IMS) in 2013.

Ramzi Darraji (Member, IEEE) received the Ph.D. degree in electrical engineering from the University of Calgary, Calgary, AB, Canada, in 2013.

He is currently with Renesas Electronics Corporation, Ottawa, ON, Canada, pursuing research and product development of advanced power amplifier circuits and systems for cellular and wireless communication infrastructure. He holds three U.S. patents and has authored and coauthored over 50 refereed publications relating to radio frequency (RF) transmitter architectures, waveform-engineered and load modulated power amplifiers, and digital signal processing techniques for wireless transceivers.

Dr. Darraji was a recipient of the Natural Sciences and Engineering Research Council of Canada Post-Doctoral Fellowship, the Alberta Innovates Technology Future Doctoral Scholarship, the IEEE Microwave Theory and Techniques Society High Achievement Award, and the IEEE Wireless and Microwave Technology Conference Best Paper Award.

Sagar K. Dhar (Member, IEEE) received the Ph.D. degree in electrical and computer engineering at the iRadio Laboratory, University of Calgary, Calgary, AB, Canada, in 2020.

He is currently with Renesas Electronics, San Diego, CA, USA, working as a Staff RF Design Engineer developing power amplifiers (PAs) for 5G infrastructures. He also worked as a Sr. RF Application Design Engineer at Macom Technologies Canada Inc., Burlington, ON, Canada, developing high-efficiency/linear PAs for high power base station requirement. His current research interests include high-efficiency RF power amplifiers, Doherty power amplifiers, large-signal device modeling, digital signal processing, and load–pull techniques.

Dr. Dhar was a recipient of the Izaak Walton Killam Pre-Doctoral Scholarship, the AITF Doctoral Scholarship, the Open Doctoral Scholarship, the Transformative Talent Internship Award, the Academic Excellence Award, and the Research Productivity Award.

Tushar Sharma (Member, IEEE) received the Ph.D. degree in electrical engineering from the University of Calgary, Calgary, AB, Canada, in 2018.

He did his postdoctoral research at the Integrated Micro-Systems Research Laboratory, Princeton University, Princeton, NJ, USA. He is currently a Staff RF Engineer at Renesas Electronics, San Diego, CA, USA, and a Visiting Professor at the Indian Institute of Technology Bombay, Bombay, India. He has more than 45 publications in international journals and conferences along with four granted patents. His research interests include high-frequency novel reconfigurable techniques in RF and mm-wave transmitters, broadband high-power gallium nitride (GaN) power amplifiers, large-signal device modeling, technology characterization, digital signal processing, mm-wave amplifiers, and waveform engineering.

Dr. Sharma was a recipient of the IMS 2020 Best Industry Paper Award, the 2019/2020 IMS Best Student Paper Award, the Izaak Walton Killam Pre-Doctoral Scholarship, the Alberta Science and Innovation under 30 Future Leader Award, the Alberta Innovates Technology Future Doctoral Scholarship, the Alberta Transformative Talent Scholarship, the IEEE Education Activity Board Pre-Educator Award, IEEE MGA Young Professionals Achievement Award, and the University of Calgary 2018 Early Achievement Alumni Award.

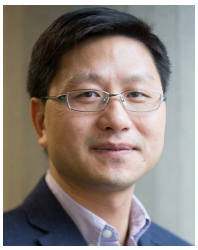

Anding Zhu (Fellow, IEEE) received the Ph.D. degree in electronic engineering from the University College Dublin (UCD), Dublin, Ireland, in 2004.

He is currently a Professor with the School of Electrical and Electronic Engineering, UCD. His research interests include high-frequency nonlinear system modeling and device characterization techniques, high-efficiency power amplifier design, wireless transmitter architectures, digital signal processing, and nonlinear system identification algorithms.

Prof. Zhu is an Elected Member of the IEEE Microwave Theory and Technology Society (MTT-S) Administrative Committee (AdCom) and a member of the IEEE Future Directions Committee. He was a recipient of the 2021 IEEE MTT-S Microwave Prize. He served as the Secretary for the IEEE MTT-S AdCom in 2018 and the Chair for the IEEE MTT-S Microwave High-Power Techniques Committee (TC-12) in 2020 and 2021. He is a Track Editor of IEEE TRANSACTIONS ON MICROWAVE THEORY AND TECHNIQUES and an Associate Editor of *IEEE Microwave Magazine*.